



Comparative investigations of structural, electronic, optical, and thermoelectric properties of pure and 2 at. % Al-doped ZnO

Nozha El Ahlem Doghmane¹ · Sabah Chettibi¹ · Malika Doghmane¹ · Djemâa Ben Othmane² · Tahar Touam²

Received: 14 July 2023 / Accepted: 9 October 2023 / Published online: 17 October 2023
© The Author(s), under exclusive licence to Springer-Verlag GmbH Germany, part of Springer Nature 2023

Abstract

Context We comparatively investigate the properties of pure ZnO and 2 at. % Al doping concentration of ZnO, AZO, as potential candidates for specific applications.

Methods Calculations were carried out, using Wien2k package, to deduce structural, electronic, optical thermoelectric, and properties of both ZnO and AZO materials via the combination of GGA and mBJ approximations.

Results It is shown that Al doping of ZnO (AZO) improves its optical properties; the deduced direct fundamental gap is enhanced due to the Burstein–Moss effect. Moreover, the dielectric function, at lower energies, confirms the existence of an extra strong fluctuation in the dispersive real part $\epsilon_1(\omega)$ and a high peak for absorptive imaginary parts $\epsilon_2(\omega)$ which are due to a variation in specific molecular bonding and the transition between the occupied and the non-occupied states. The critical point, observed at 2.81 eV for pure ZnO, is shifted to 3.3 eV in 2 at. % AZO, confirming a larger optical band gap. The reflectivity values slightly decreased for 2% AZO. The investigation of thermoelectric parameters as a function of chemical potential at different temperatures ranging from 300 to 900°C showed that these structures can be considered for good thermoelectric devices with (i) high absolute values of Seebeck coefficient: $|S_{ZnO}| = 1.16$ mV/K and $|S_{AZO}| = 0.746$ mV/K, (ii) no effect of temperature on electrical conductivity but a strong effect on thermal conductivity, (iii) a high value approaching unity for the figure of merit. Hence, these properties and their improvements, introduced by Al doping of ZnO, lead specific and more uses in optoelectronics, energy, and piezoelectric applications.

Keywords ZnO · AZO · Wien2k · GGA-mBJ

Introduction

In order to develop new technological applications to cope with the improvement of people's living standards, novel approaches based on low-cost, efficient, ecofriendly, and good physical semiconductor properties are becoming a global priority and a very interesting field of research. Nowadays, the most promising materials for such purposes are wide band gap semiconductors, in particular the new class of transparent conducting oxides (TCO) that exhibit both

transparency and electronic conductivity simultaneously. In fact, TCOs are characterized by remarkable and multifunctional properties such as larger band gap, higher electron mobility, higher carrier density, and higher breakdown field strength. Thus, several TCO devices can be designed for many applications: high power and high temperature electronic devices, sensor devices, solar cells, displays transparent electronics, short wavelength optoelectronics, spintronics, photocatalysis, etc. [1–5].

Among these TCOs, zinc oxide (ZnO), a direct band gap semiconductor with a significant exciton binding energy and high optical gain at ambient temperature and other distinctive properties, is receiving a great deal of fundamental and applied research interest all over the world [6–9]. Indeed, it is one of the most promising II–VI binary semiconductors for several potential applications in numerous fields such as energy storage, electronics, optoelectronics, and environment photocatalysis [10–14]. ZnO possess different important characteristics with high transparency, anti-radiation

✉ Tahar Touam
touamt@gmail.com

¹ Laboratoire de Physique des Matériaux, L2PM, Département Sciences de la Matière, Faculté MISM, Université 08 Mai 1945, DZ-24000 Guelma, Algeria

² Laboratoire des Semi-conducteurs, Département de Physique, Faculté des Sciences, Université Badji-Mokhtar-Annaba, B.P 12, DZ-23000 Annaba, Algeria

stability, large specific area, strong ultraviolet excitation, good compatibility, piezo-electricity at room temperature, and a high isoelectric point [15, 16]. Furthermore, with its great thermal and mechanical stability, oxidation resistance, affordability, and non-toxicity, ZnO is one of the viable candidates for thermoelectric materials. Such materials are of great importance in space applications (radioisotope thermoelectric generators) and in solar-thermal-electrical-energy production. Indeed, thermoelectric power is being considered as alternative renewable and green energy [17, 18]. This wide band gap semiconductor exists in several interesting polymorphs among which the three main phases are wurtzite (WZ), rock salt (RS), and zinc blende (ZB) structures. The WZ structure, with an ionicity lying between that of covalent and ionic materials, is the most thermodynamically stable phase at the ambient conditions [19–21].

Moreover, ZnO can be doped and/or co-doped, n- or p-types, with several metallic and nonmetallic elements from different groups such as transition metal, noble metals, and rare-earth elements, e.g., Al, Ag, B, Bi, Ce, Co, Cr, Cu, Dy, Er, Eu, F, Fe, Ga, In, La, Li, Mg, Mn, Mo, N, Nb, Nd, Ni, P, Pm, Pr, Sb, Sm, Sn, S, and Y [22–36]. The advantages of the incorporation of dopants, which act as donors or acceptors, reside in the improvement of electrical and optical properties via the generation of excess mobile free carriers (electrons or holes) as well as in the changes introduced in the band gap energy as a result of the generation of lattice defects in the material structure [37]. The control of ZnO different properties, via doping, leads to the design of new devices and more fields of applications. Aluminum, Al, a cheap, durable, abundant, and non-toxic metal belonging to the group III elements, is considered to be the most promising dopant in ZnO due to the improvement of its properties and to mass production applications in photovoltaic devices, organic light-emitting diodes, sensors, optoelectronics and liquid crystal display. Hence, Al-doped zinc oxide, AZO, characterized by a high conductivity and a good optical transmission, has proved to be an excellent TCO material. It is attracting a considerable attention for transparent conducting electrodes in replacement of the widely used commercial indium tin oxide (ITO) electrodes and other applications in solar cells, liquid crystal displays, window layers, etc. [38–42].

Thus, fundamental understanding of different properties of both ZnO and AZO semiconductors, are necessary to improve their performances, as base materials, in electronics and optoelectronics devices as well as in piezoelectric and energy applications. However, the choice of the appropriate method and the adequate conditions to study this material still represents a great challenge to get accurate results in less investigation time. Although, several experimental and theoretical approaches are being developed to determine the AZO properties [43–47], there is still a lack of studies of

low Al doping, in particular the 2 at. % Al doping, with a very few experimental studies and an absence of theoretical investigations.

In this context, using Wien2k package [48], we numerically deduce structural, electronic optical and thermoelectric properties of pure wurtzite ZnO, as a reference material, and Al doping concentration of 2.0 at. % of ZnO. Then, keeping in mind the comparative aspects, we carry out a discussion to put into evidence the differences and the improvements in different properties of pure and doped ZnO.

Computational methods

For calculation processing and data collection, we used the code Wien2k package that employs the density functional theory, DFT, based on the full potential linearized augmented-plane wave, FP-LAPW method. In order to deduce the best approximations that improve the results, in less time calculations, we first tested for wurtzite ZnO different approximation: local density approximation, LDA,

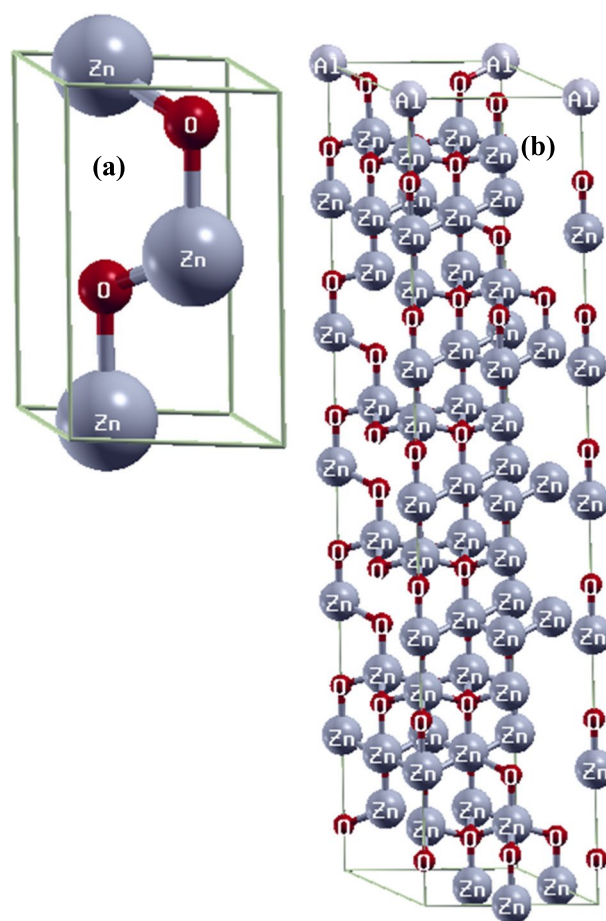


Fig. 1 Unit cells of **a** the wurtzite (B4) phase of ZnO and **b** the structure of $(2 \times 2 \times 6)$ supercell $\text{Zn}_{0.98}\text{Al}_{0.02}\text{O}$

WC-GGA, PBEsol-GGA, PBE-GGA, etc. Then, to carry out all properties calculations, we opted for generalized gradient approximation, GGA [49], for structural properties determination, and the modified Becke-Johnson, TB-mBJ [50], for electronic and optical properties deductions. The combination of such approximations gives more accurate semiconductor band gap values for several semiconductors and insulators [50, 51]. Prior to any property determination, we confirmed the optimization and the stability of the structure which plays an important role in computational calculations of materials' physical properties. The X-ray diffraction, XRD, patterns were determined by VESTA and for the thermoelectric properties, we used the BoltzTrap code [52, 53]. Thus, we investigated the most stable WZ-ZnO phase doped with 2% aluminum metal. In the calculation, the basis atom set locations were (1/3, 2/3, 0), (2/3, 1/3, 1/2) for Zn and (1/3, 2/3, 3/8), (2/3, 1/3, 7/8) for O [54, 55], and the initial experimental lattice parameters: $a = b = 3.25$ and $c = 5.207$ [56].

The crystal geometry of ZnO that exhibits, in ground state, a stable hexagonal wurtzite structure is considered to be the energetically most favorable as compared to other phases [20]. The unit cells of the wurtzite (B4) phase of pure ZnO is illustrated in Fig. 1a; the Zn and O atoms are marked in the schematic with grey and red circles, respectively. WZ unit cell that belongs to the space group 186 P63mc consists of two zinc atoms and two oxygen atoms. Figure 1b illustrates the adopted hexagonal $2 \times 2 \times 6$ supercell which includes 48 oxygen atoms and 48 zinc atom into which one Zn atom is substituted by an Al atom; thus corresponding to ~ 2% at. Al concentration, i.e., $\text{Zn}_{1-x}\text{Al}_x\text{O}$ (with exactly $x = 0.02083$).

In order to get a good energy convergence of pure and doped ZnO, the convergence test was performed; it gave a cutoff energy equal to 350 eV according to convergence accuracy. 512 and 200 k-points were used for pure and doped ZnO, respectively. The adopted cutoff wave vector

in the interstitial region was $R_{\text{MT}} \times K_{\text{max}} = 8$, where R_{MT} is muffin-tin radius and k_{max} is the maximum wave vector in the reciprocal lattice. To study the stability of this structure, after doping, we calculated its formation energy that depends on the total energies of pure (E_{pure}) and Al-doped ZnO (E_{doped}) as well as the chemical potentials of Zn (μ_{Zn}) and Al (μ_{Al}), such as [34]:

$$E_f = E_{\text{doped}}(\text{Al}_{(\text{Zn})}) - [E_{\text{pure}}(\text{ZnO}) - \mu_{\text{Zn}} + \mu_{\text{Al}}] \quad (1)$$

Thus, the calculated formation energy was found to be -2.5 eV; this negative value indicates and ensures that this material is stable

Results and discussion

Structural properties

In order to study the material stability, all optimization calculations were carried out with structure relaxation. Geometry minimization was also achieved via the calculation of the total energy as a function of unit cell volume; this procedure is necessary to obtain the minimum energy that puts into evidence the stability of both ZnO and AZO. The calculated values of the optimized lattice constants for ZnO are found to be $a = b = 3.2856$ Å, $c = 5.311$ Å, and $c/a = 1.616$, which are consistent with values previously reported experimentally and theoretically [54, 57–61].

The determination of equilibrium volume, V_0 , ground state energy, E_0 , bulk modulus at pressure $P = 0$, B_0 , pressure derivative of bulk modulus, B_0' are carried out by fitting the total energy as a function of the reduced and extended volume of the unit cell into third-order Birch–Murnaghan's equation of state. Thus, the total energy, $E(V)$, and pressure $P(V)$ as a function of volume are given by [62]:

$$E(V) = E_0 + \frac{9V_0B_0}{16} \left\{ \left[\left(\frac{V_0}{V} \right)^{\frac{2}{3}} - 1 \right]^3 B_0 + \left[\left(\frac{V_0}{V} \right)^{\frac{2}{3}} - 1 \right]^2 \times \left[6 - 4 \left(\frac{V_0}{V} \right)^{\frac{2}{3}} \right] \right\} \quad (2)$$

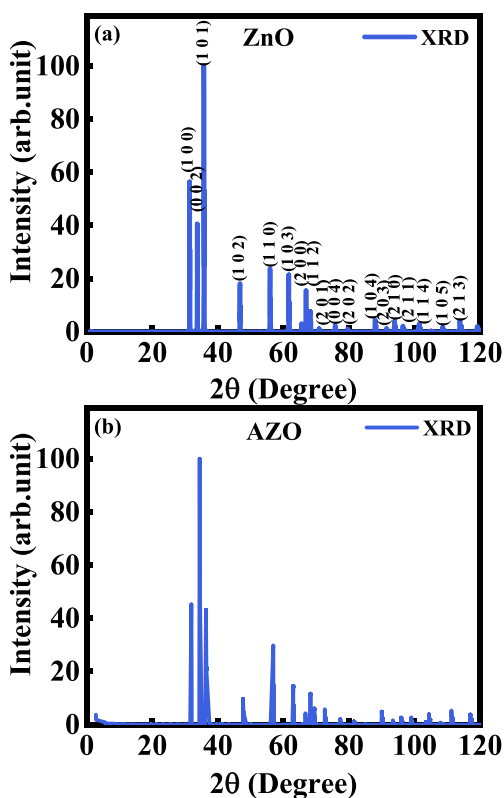
$$P(V) = \frac{3B_0}{2} \left[\left[\left(\frac{V_0}{V} \right)^{\frac{2}{3}} - \left(\frac{V_0}{V} \right)^{\frac{5}{3}} \right] \right] \times \left\{ 1 + \frac{3}{4}(B_0 - 4) \left[\left(\frac{V_0}{V} \right)^{\frac{2}{3}} - 1 \right] \right\} \quad (3)$$

Thus, the other deduced parameters B, B', and V were also found to be in agreement with published data [62–66] obtained with different

experimental techniques (X-ray diffraction, XRD, extended X-ray absorption fine structure, EXAFS and Mossbauer) and computing methods. The similarities in the values for

Table 1 Deduced and reported [62–66] parameters of pure ZnO and 2 at. % AZO

Parameters	Pure ZnO				2 at. % AZO			
	This work	Experimental		Calculated	Methods	This work		
		GGA	Techniques					
B (GPa)	127,37	142.6 [63]	XRD	128.72 [62]	GGA	193.251		
		173 [64]	XRD				129.73 [65]	GGA EV
		183 [66]	EXAFS.					
B'	4,8726	4 [66]	XRD + Mössbauer	4.38 [62]	GGA	4.03		
		4 [64]	XRD	4.68 [65]	GGA EV			
V(Å) ³	24.828	23.796 [66]	XRD + Mössbauer	24.61 [62]	GGA	23.513		
		23.81 [63]	XRD				24.939 [65]	GGA EV
		23.99 [64]	XRD + EXAFS					
a (Å)	3.2856	3.2496 [66]	XRD + Mössbauer	3.286 [62]	GGA	3.23215		
		3.2498 [63]	XRD					
		3.25 [64]	XRD + EXAFS					
c (Å)	5.3114	5.2042 [66]	XRD + Mössbauer XRD	5.269 [62]	GGA	5.1978		
		5.2066 [63]	XRD + EXAFS					
		5.220 [64]						

**Fig. 2** XRD patterns of **a** pure ZnO and **b** 2 at. % AZO

ZnO indicate the reliability and the validity of the present chosen approximations and consequently can safely be used for the 2 % at. Al doping concentrations of AZO. It can also be noticed from Table 1 that the decrease in the AZO cell parameters leads to a decrease in the supercell volume as a result of the large difference in electronegativity and atomic radii of Zn and Al atoms.

Moreover, XRD patterns were also numerically calculated with VESTA code [52]. The obtained results are displayed in Fig. 2 for ZnO and 2 at. % AZO. The peaks indexations, when compared to the standard powder diffraction patterns (JCPDS card no. 36-1451), confirm the hexagonality of these materials. Several intensive peaks, located at different 2θ values, are observed. The ZnO and 2 at. % AZO spectra are very similar in peak positions and quite different in peak intensities. However, a close analysis would show that, for example, the intensive peaks located at different 2θ values, such as 31.49° , 33.81° , and 35.77° in ZnO spectra shifted towards higher 2θ values, i.e., =, 31.94° , 34.42° , and 36.43° in AZO. The slight shift, also observed experimentally in literature for similar and higher Al-doping concentrations [67, 68], confirms the existence of a decrease in the cell constant with the incorporation of the concentration of Al dopant. In fact, the ionic radius of Al^{3+} is less than that of Zn^{2+} which leads to a decrease in the cell constants.

Electronic properties

The calculation of the band structure and its corresponding density of states (DOS) generally reflect the electronic tendency of a given material; this would be interesting and practical in device designs. Since DFT approximations underestimate the gap calculations [69] all the following results are obtained by GGA and mBJ combination. Thus, Fig. 3 illustrates the computed energy band structures obtained for pure ZnO (Fig. 3a) and 2 at. % AZO (Fig. 3b). It is clear that the valance band maximum, *VBM*, is exactly situated beneath the conduction band minimum, *CBM*, at the same high symmetry $\Gamma(0, 0, 0)$ point of the first Brillouin zone. Thus, the ZnO is a direct band gap semiconductor, E_g , with a deduced value of its fundamental gap equals to 2.81

Fig. 3 Calculated electronic band structure of **a** pure ZnO and **b** 2 at. % AZO. The Fermi level is set at $E = 0$ eV

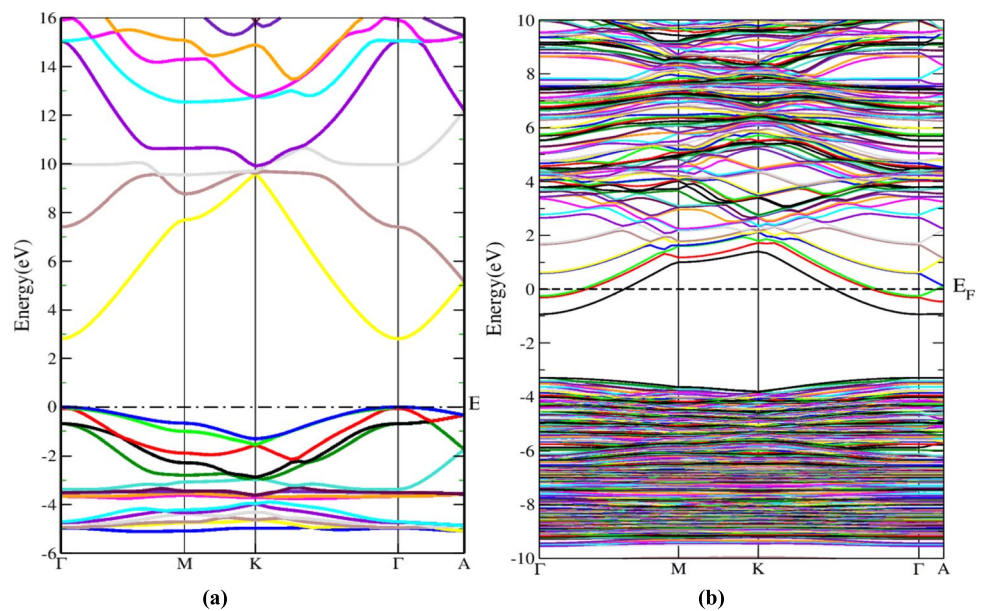


Table 2 Deduced and reported energy band gap of pure ZnO [8, 21, 70–74], and 2 at. % AZO [75]

	Pure ZnO				2 at. % Al-doped ZnO			
	This work	Experimental		Calculated		This work	Exp.	Calc.
	GGA-mBJ	Gap	Technique	Gap	Methods	GGA-mBJ		
Energy gap (eV)	2.81	3.3 [8]		2.58 [71]	GGA-mBJ	3.3	3.30 [75]	/
		3.2 [70]	Spectro/ellipsom.	1.00 [72]	LDA+GW			
		3.05 [70]	UV-Vis.	2.49 [73]	HSE			
		3.28 [35]	UV-Vis.	2.59 [74]	LDA mBJ			

eV. This value, though relatively lower than that determined experimentally [70], it is better than other reported approximations, such as GGA-mBJ [71], LDA+GW [72], HSE [73], and LDA mBJ [74] (Table 2).

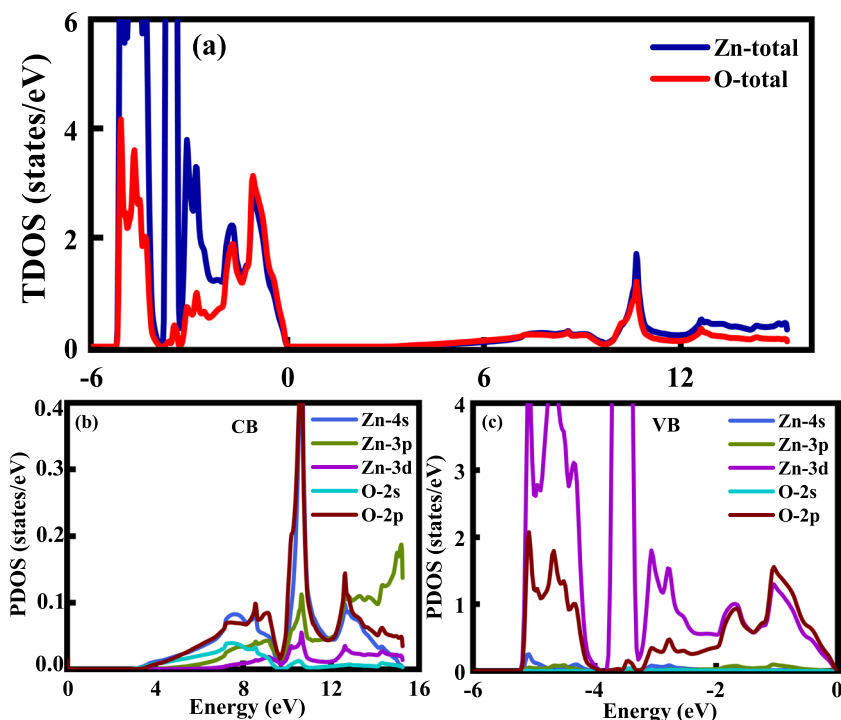
The doping effect is put into evidence in Fig. 3b for 2 at. % AZO; one can easily make several observations: (i) a redistribution of the energy band structure, (ii) a shift of Fermi level into the conduction band, (iii) the direct band gap is situated at the same Γ point as pure ZnO, and (iv) the energy band gap is changed. It should be noted that Al dopants in ZnO structure act as donors and consequently AZO behaves as an n-type semiconductor. A hybridization is noticed when going from the Γ center towards M ($1/2, 0, 1/2$) and from K ($2/3, 1/3, 0$) towards Γ ($0, 0, 0$); hybridization occurs between M and K and between Γ and A ($1/3, 2/3, 1/2$).

Moreover, it can be seen that the Fermi level is located within the conduction band. To explain this physical phenomenon, we know that as the doping of a semiconductor with donor impurities increases, the Fermi level shifts from the energy mid-gap (in the intrinsic case) towards the conduction band. When the doping concentrations reach very

high levels, E_f not only attains the CBM but also penetrates in the conduction band leading to what is known as degenerate semiconductors.

This physical phenomenon, also known as Moss–Burstein, occurs when some of the lowest states of the conduction band are filled (i.e., the CB becomes partially filled). This situation is clearly visible in the present 2 at. % AZO energy band structure (Fig. 3b) for which the Fermi level, E_f , is located into the CB. In fact, the optical band gap, from E_f to VBM is larger than the fundamental gap by an amount known as the Moss–Burstein shift [76–78]; i.e., this shift widens the optical band gap. Thus, the 2 at. % Al doping of ZnO raises the Fermi level above the CBM and widens the optical band gap to become 3.3 eV. This value is in very good agreement with that determined experimentally, 3.3 eV, for the AZO thin films prepared by sol-gel technique with the same Al doping concentration of 2.0 at. % [75]. A comparable result of 2.26 eV was also reported for 3.0 at. % AZO prepared by the spin coating method [35]. The broadening of the optical band gap of Al-doped zinc oxide compared to pure ZnO films was attributed to Moss–Burstein shift that appears in heavily doped

Fig. 4 Calculated TDOS (a) and PDOS (b and c) of pure ZnO



ZnO films. It should be noted that the increase in the optical gap improves simultaneously both electrical conductivity and optical transparency [75, 79] and consequently opens up other prospects in optoelectronics.

The total density of states, TDOS, and partial density of states, PDOS, give an increased understanding of the contribution of different states to the energy bands. Figure 4 illustrates TDOS and PDOS of pure ZnO. The whole DOS spectrum (Fig. 4a) shows the variations in both valence band [−6e−0 V] and conduction band [2.81–16 eV] separated by an energy gap equal to 2.81 eV. The conduction band (Fig. 4b) consists mainly of 4s states of zinc and 2p states of oxygen, followed by a strong hybridization between Zn-3p, Zn-3d, and O-2p. These results are in agreement with literature [42, 80]. For the valence band (Fig. 4c), it can clearly be seen that the DOS curves can be divided into three regions:

- The first region (from −5.2 to −3.8 eV) shows a strong contribution of Zn-3d together with a weak contribution of O-2p.
- The second region (−3.8 to −3.2 eV) comes mainly from the Zn-3d.
- The third region (from −3.2 to 0eV) is the result of a mixture of O-2p and Zn-3d states and a small amount of Zn-3p states. This is principally due a p-d hybridization of O-p and Zn-d states

The obtained results of the total and partial density of states as a function of energy for 2 at. % AZO are shown in Fig. 5. The valence band, in the energy range (−10.4 to −9.6 eV),

consists of O-2p, Zn-3d, and Al-2s; whereas, in the range (−9.6 to −3.38 eV), its nature is mainly Zn-3d and O-2p. The bottom of the conduction band is due to a hybridization between the atomic orbitals Zn-4s and O-2p followed by Zn-4p and Al-3s states for higher energies. The Al doping of ZnO leads to a shift of the Fermi level above the conduction band and consequently the donor energy level into the CB. This behavior indicates that 2 at. % Al-doped ZnO is a degenerate n-type semiconductor, which confirms the above band structure results (Fig. 3b). In fact, the incorporation of Al dopants into the ZnO structure produces free electrons leading to higher carrier concentration and consequently higher conductivities.

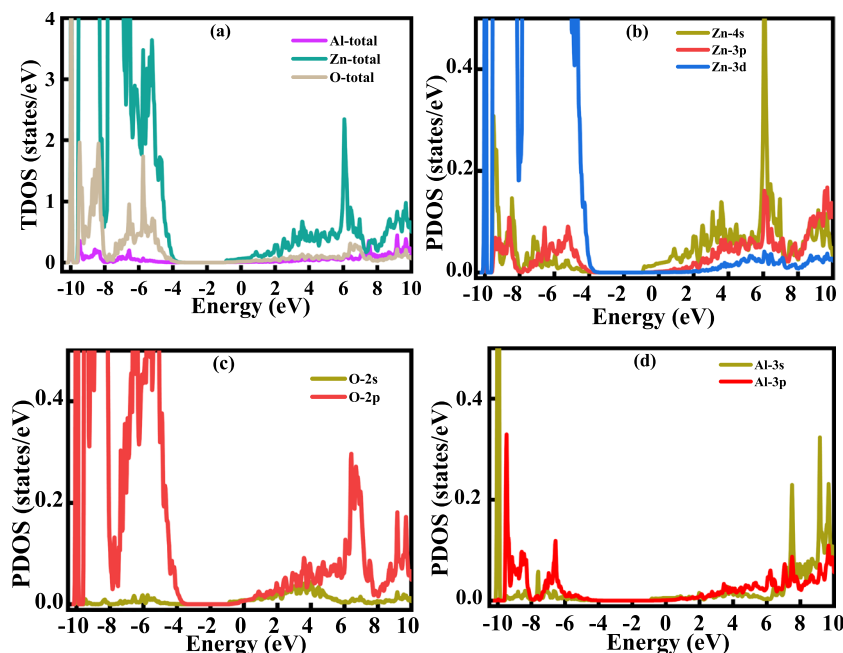
Optical properties

The semiconductor optical properties form the milestone of any device design and fabrication for thin film applications, in particular in optoelectronics and photoelectronics. The determination and understanding of such properties requires the investigation of some optical parameters, individually or altogether, such as: dielectric function, $\epsilon(\omega)$, reflectivity, $R(\omega)$, absorption coefficient $\alpha(\omega)$ refractive index, $n(\omega)$, extinction coefficient $k(\omega)$, and conductivity, $\sigma(\omega)$ [42, 71, 81–84].

Dielectric function

The complex dielectric function, which describes the linear response of macroscopic optical properties of a solid, is usually given by:

Fig. 5 Calculated TDOS (a) and PDOS (b, c, and d) of 2 at. % AZO



$$\varepsilon(\omega) = \varepsilon_1(\omega) + \varepsilon_2(\omega) \quad (4)$$

where $\varepsilon_1(\omega)$ is the real part that represents the dispersion of the incident photons by the materials and $\varepsilon_2(\omega)$ is the absorptive imaginary parts of the complex dielectric function. The imaginary part, $\varepsilon_2(\omega)$, is given by the following expression:

$$\varepsilon_2(\omega) = \left(\frac{4\pi^2 e^2}{m^2 \omega^2} \right) \sum_{ij} \int \langle i|M|j \rangle^2 f_i (1 - f_j) \delta(E_j - E_i - \omega) d^3k \quad (5)$$

where ω is the incident photon energy frequency, e is the electronic charge, M is the dipole matrix, i and j are the initial and final states, respectively, f_i is the Fermi distribution as a function of the i th state, and E_i is the energy of electron in the i th state.

The real part $\varepsilon_1(\omega)$ can be calculated from the imaginary part by using the Kramers–Kronig's equation [82–84]:

$$\varepsilon_1(\omega) = 1 + \frac{2}{\pi} p \int_0^\infty \frac{\omega' \varepsilon_2(\omega')}{\omega'^2 - \omega^2} d\omega' \quad (6)$$

where p indicates the main value of integral. The knowledge of the dielectric function is essential for the determination of other optical parameters: $R(\omega)$, $n(\omega)$, $k(\omega)$, and $\alpha(\omega)$. Since wurtzite ZnO possesses a hexagonal symmetry, one has to calculate two different independent principal components for $\varepsilon(\omega)$ so that $\varepsilon_{zz}(\omega)$ and $\varepsilon_{xx}(\omega)$ correspond to parallel- and perpendicular- polarization of c-axis, respectively. Hence, the comparison between optical parameters should be carried out in both directions.

Figure 6 illustrates the calculated real and imaginary parts of the dielectric function of pure and 2 at. % AZO. From Fig. 6a,

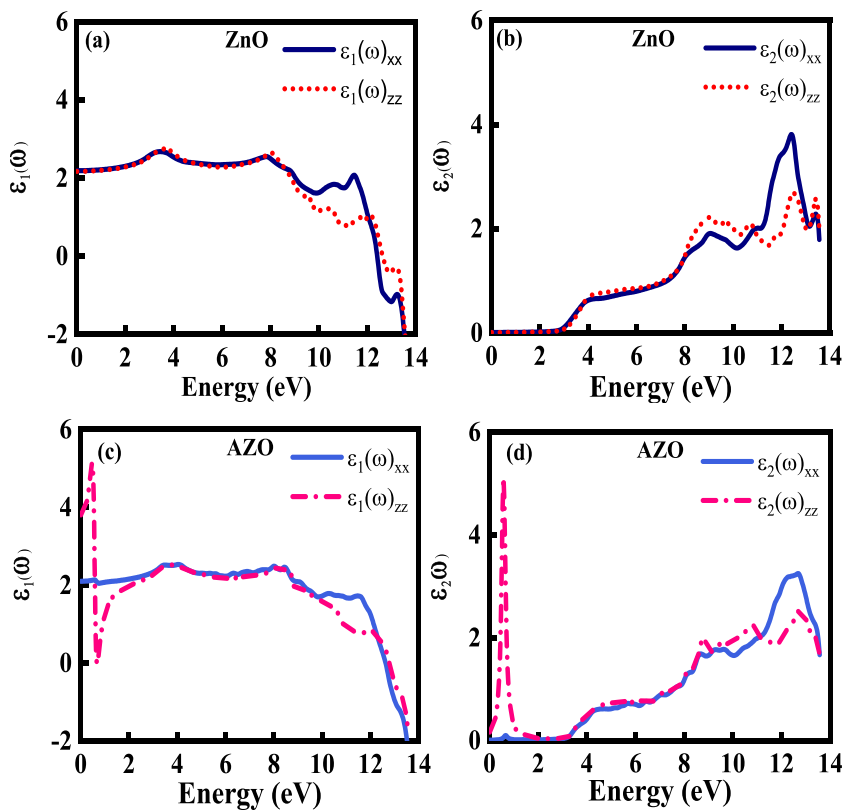
which shows the real part of $\varepsilon_1(\omega)$ of pure ZnO, it can be seen that as the energy increases, we observe a fluctuation at 3.63 eV for $\varepsilon_1(\omega)_{xx}$ and $\varepsilon_1(\omega)_{zz}$, whose onset corresponds to a first critical point situated at 2.81 eV. This critical point is also obtained in Fig. 6b for the $\varepsilon_2(\omega)$ versus energy curves; it can easily be noticed that the onset of the curves increase occurs at the same critical point situated at 2.81 eV. This point, which represents $\Gamma_C - \Gamma_V$ separation, indicates the onset (threshold) of direct optical transitions between the valence band maximum and the first minimum conduction band. This is known as the threshold of the fundamental absorption that corresponds to the fundamental energy gap, confirming that deduced above, 2.81 eV.

Moreover, we also notice an important anisotropy in both real and imaginary parts of the dielectric function beyond 8.2 eV, whereas they possess an isotropic behavior for lower energies. This anisotropy in optical properties is expected for low symmetry crystals. However, for 2 at. % AZO, (Fig. 6c and d), we can notice two main and important differences with pure ZnO.

- At lower energies the appearance of (i) an extra strong fluctuation in $\varepsilon_1(\omega)$ versus energy curves and a (ii) high peak for $\varepsilon_2(\omega) = f(E)$ curves. This phenomenon is due to a variation in specific molecular bonding, the transition between the occupied states beneath the Fermi level and the non-occupied states above E_f in the conduction band.

The critical point (at 2.81 eV for pure ZnO) is shifted to 3.3 eV in 2 at. % AZO, indicating a transition from the valence band to the partially filled CB; this situation corresponds to the Moss–Burstein effect that leads to the shift of E_f in CB and to a larger optical band gap

Fig. 6 Calculated real and imaginary parts of dielectric function: **a** and **b** pure ZnO and **c** and **d** 2 at. % AZO



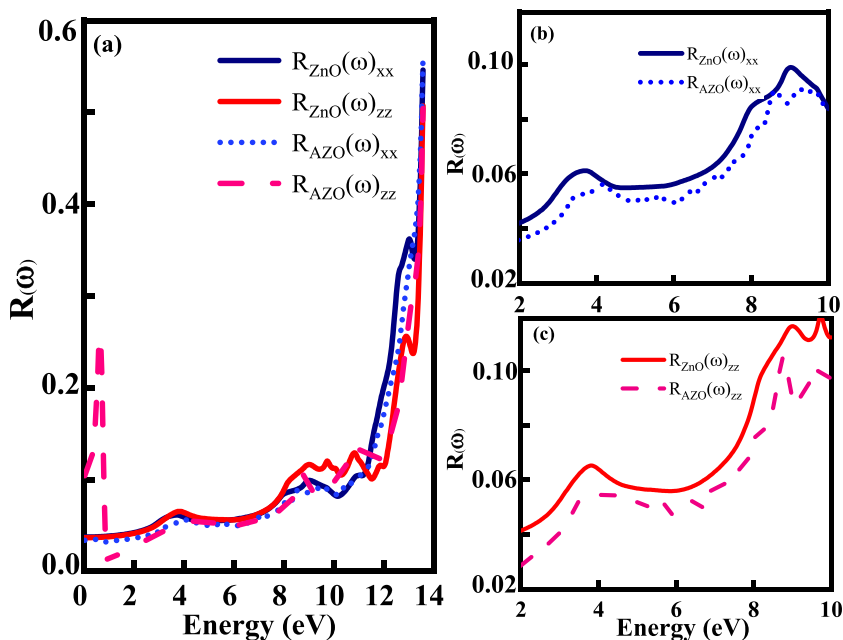
Reflectivity

$$R(\omega) = \left[\frac{\sqrt{\epsilon(\omega)} - 1}{\sqrt{\epsilon(\omega)} + 1} \right]^2 \tag{7}$$

The reflectivity depends on the dielectric function according to the equation [82, 83]:

Figure 7a represents the reflectivity as a function of energy for pure and 2 at. % AZO for $R(\omega)_{xx}$ and $R(\omega)_{zz}$. It

Fig. 7 (a) Relationship between reflectivity with energy for pure ZnO and 2 at. % AZO and (b) and (c) enlarged reflectivity in 2-10 eV range



can be observed that, in all cases, the overall tendency is that, the reflectivity intensifies very slowly up to 11 eV and then strongly increases beyond this value. However, compared to pure ZnO, we notice the appearance in the AZO reflectivity a new high peak with $R(\omega)_{zz}$ curve at 0.96 eV, which could be due to the new impurity band introduced by Al doping. This is consistent with the preceding observation and analysis of the imaginary part of the dielectric function.

Moreover, the doping effect seems to slightly lower the reflectivity values for both polarization directions, this is better illustrated in the enlarged (Fig. 7b and c). In fact, e.g., at $E = 2$ eV, $R(\omega)$ decreases from $R_{\text{ZnO}}(\omega)_{xx} = 0.04212$ and $R_{\text{ZnO}}(\omega)_{zz} = 0.04138$ for ZnO to $R_{\text{AZO}}(\omega)_{xx} = 0.03602$ and $R_{\text{AZO}}(\omega)_{zz} = 0.02866$ for AZO, respectively. This reflectivity decrease corresponds to ~ 1.17 for xx-polarization and ~ 1.45 for zz-polarization. This is a positive effect since it achieves a lower reflectivity. It should be noted that a TCO should have a low reflectivity for its use in various optoelectronic applications [43]. This tendency is in agreement with reported experimental [75] and theoretical works [85]. In fact, the reflectivity of 6 at. % AZO was found to be about twice less than that of pure ZnO [85].

Absorption coefficient

The absorption coefficient, $\alpha(\omega)$, an important factor for the evaluation of material optical properties, is a function that can measure the material ability to absorb the energy. This parameter depends on the dielectric function as follows [82].

$$\alpha(\omega) = \sqrt{2}\omega \left[\sqrt{\varepsilon_1^2(\omega) + \varepsilon_2^2(\omega)} - \varepsilon_1(\omega) \right]^{1/2} \quad (8)$$

Figure 8 illustrates the absorption coefficient as a function of energy for (a) pure and (b) 2% AZO for $\alpha(\omega)_{xx}$ and $\alpha(\omega)_{zz}$. Several observations can easily be made, namely:

- The absorption coefficient of both pure and 2 at. % AZO is very weak in the range of visible spectrum, indicating a high transmission in this region.

- Pure ZnO, absorbs above 2.81 eV, i.e., in the UV and beyond
- The anisotropy phenomenon sets in for energies higher than 8.2 eV, beyond which an important absorption is observed around 9.2 eV along zz and at 10.1 eV along xx.
- the appearance in AZO of a new high peak with $\alpha(\omega)_{zz}$ curve at 0.96 eV, confirming the previously obtained peak with reflectivity,
- For 2 at. % AZO, the absorption coefficient is higher than that of pure ZnO in the range [3.1–6.2eV]. It can also be seen that an important absorption (strong peak) along the zz direction occurs in the IR. Moreover, compared to pure ZnO, a small blue shift phenomenon is obtained in the 2 at. % AZO.

All these observations can for the basis for the study and the design of specific devices as light protectors.

Thermoelectric properties

Thermoelectricity consists of converting thermal energy directly to electrical energy in solid materials. The determination and understanding of materials thermoelectric properties requires the investigation of some interrelated parameters: Seebeck coefficient, S , electrical conductivity, σ , thermal conductivity, κ , power factor, PF , and figure of merit, ZT [18, 53, 85–90].

Figure 9 illustrates the Seebeck coefficient as a function of chemical potential for (a) pure ZnO and (b) 2% at. AZO at different temperatures 300 K, 600 K, and 900 K. It is clear that the overall curve behavior is similar: a saturation, a sharp positive peak, a sharp negative peak, and a final saturation. It should be noted that positive S values indicate that the material is p-type whereas negative S values are obtained in n-type semiconductors. However, despite the similarities in curve trends several discrepancies and remarks can be made for both ZnO and AZO as follows.

Fig. 8 Relationship between absorption coefficient with energy for a pure ZnO and b 2 at. % AZO

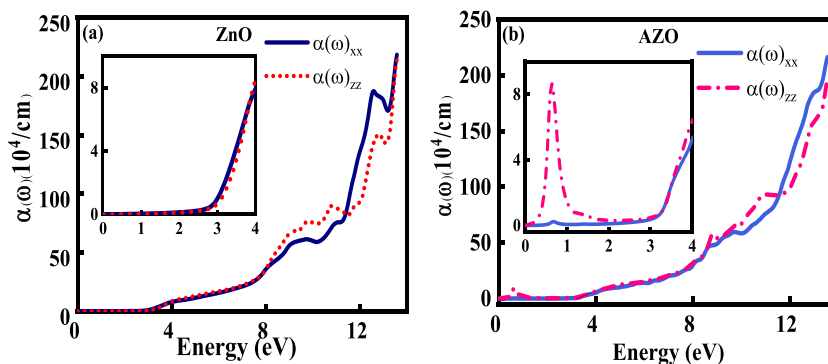
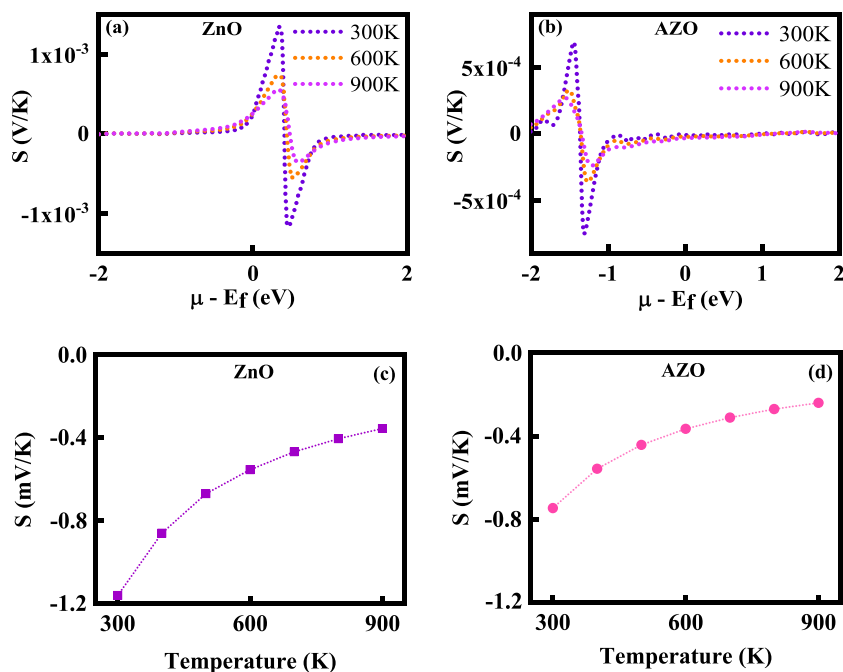


Fig. 9 Seebeck coefficient as a function of chemical potential (a and b) and temperature (c and d) of pure ZnO and 2 at. % AZO



- With increasing temperatures, the peak position very slightly shifts towards higher chemical potentials
- Compared to pure ZnO, the peak positions in AZO shifted towards lower chemical potentials around -1.5 eV.
- The highest values of Seebeck coefficient, $S_{ZnO} = 1.329$ mV/K and $S_{AZO} = 0.688$ mV/K for ZnO and 2 at. % AZO, respectively are obtained at 300 K in the p-type region. In the n-region the maximum absolute values are found to be: $S_{ZnO} = -1.16$ mV/K and $S_{AZO} = -0.746$ mV/K.
- With increasing absolute temperatures up to 900 K, the S values (peak amplitude) decrease down to $S_{ZnO} = 0.551$ mV/K and $S_{AZO} = 0.281$ mV/K for ZnO and 2 at. % AZO.

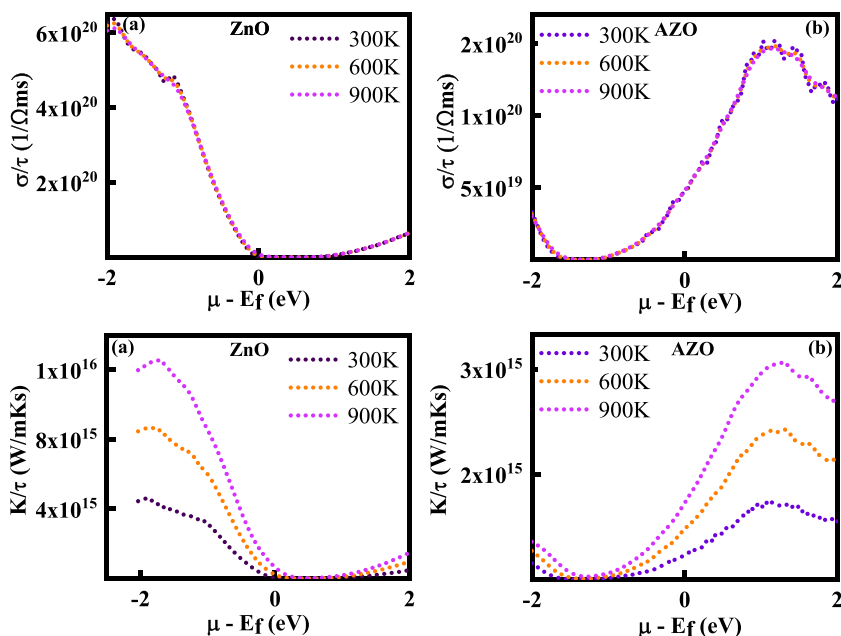
To explain the above observations, let us recall that we deduced that ZnO doping with Al leads to an n-type material and in the present case the 2 at. % AZO is shown to be a degenerate semiconductor as illustrated by its calculated electronic band structure (Fig. 3b). It can be seen that, at the high symmetry Γ (0, 0, 0) point, the conduction band minimum is located below the Fermi level (set at $E = 0$ eV). Thus, this CBM position could partly be responsible for the shift of Seebeck coefficient peak positions (Fig. 9b) below the chemical potential (at $E = 0$ eV) for the 2 at. % AZO. Therefore, for this n-type material, we only consider negative values of Seebeck coefficients. Thus, to better illustrate the temperature effects, we plot S as a function of T in the range 300 K–900 K for ZnO (Fig. 9c) and for 2 at. % AZO (Fig. 9d). The highest absolute S values are found to be $|S_{ZnO}| = 1.16$ mV/K and $|S_{AZO}| = 0.746$ mV/K, indicating that pure and doped ZnO represent good thermoelectric materials.

The evolution of electrical conductivity as a function of chemical potential is plotted in Fig. 10 for (a) pure ZnO and (b) 2% at. AZO, in terms of σ/τ where τ is the average time between two successive electron collisions [53] at different temperatures 300 K, 600 K, and 900 K. The curves show that the temperature has very negligible effect on the electrical conductivity for both materials. The lowest conductivity values, for all temperatures, are obtained in the chemical potential range of 0 to approximately 1 eV for ZnO and the range -1 to 1.75 eV for AZO.

The plots of κ/τ as a function of chemical potential are displayed in (Fig 10c, d). It can be seen that, for $T = 300$ K, the curve variation is similar to that of electrical conductivity. For ZnO (Fig. 10c), κ/τ decreases sharply in the chemical potential range of -2 to approximately 0 eV, then attains its lowest values in the range 0 to approximately 1 eV) beyond which a final increase is observed. However, the most important remark is that, unlike electrical conductivity, thermal conductivity strongly depends on temperature: as T increases, κ/τ decreases from its highest value of 2×10^{16} W/mKs at $T = 300$ K to 4.5×10^{15} W/mKs at 900 K. For 2 at. % AZO (Fig. 10d), similar remarks can be formulated: a decrease followed by the lowest saturation region is situated around -1 eV and the maximum values at ~ 1.2 eV. In fact, the κ/τ maximum decreases from $\sim 3 \times 10^{15}$ W/mKs at $T = 300$ K to 0.5×10^{15} W/mKs at 900K.

Thermoelectric power factor (PF) defines thermoelectric efficiency; it depends on Seebeck coefficient and electrical conductivity, such as $PF = \sigma S^2$. However, the need for a dimensionless parameter requires the use of the figure of merit, ZT , known as the thermal conversion efficiency, which characterizes the materials ability to convert thermal energy

Fig. 10 Electrical conductivity (a and b) and thermal conductivity (c and d) as a function of chemical potential for pure ZnO and 2 at. % AZO



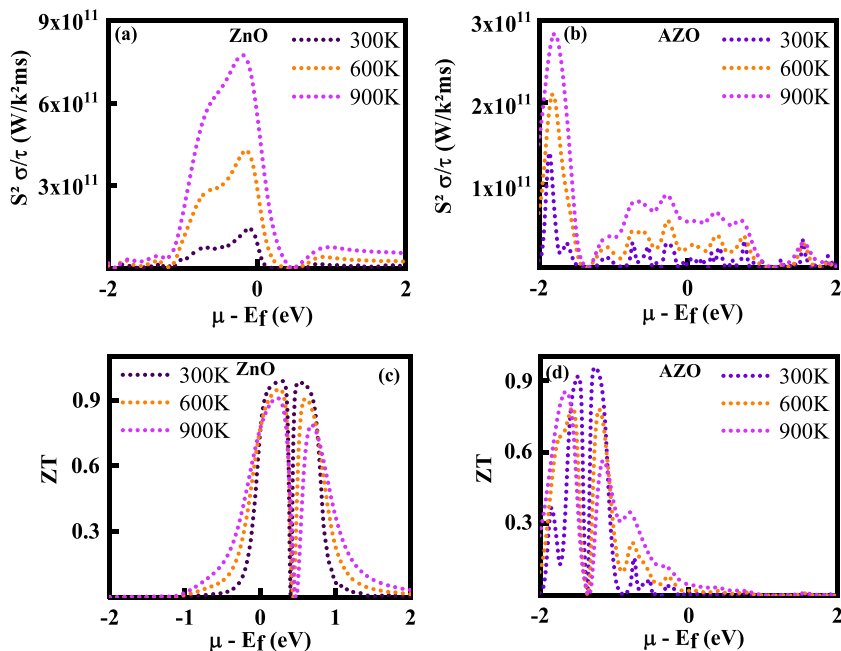
into electrical energy. It depends on the combination of three physical parameters: S , σ , and κ as well as the absolute temperature, T , according to the relation $ZT = \sigma S^2 T / \kappa$ [17, 90–92]

Figure 11a, b represents the power factor, calculated from $PF = \sigma S^2 / \tau$, as a function of chemical potential for (a) pure ZnO and (b) 2 at. % AZO at different temperatures 300 K, 600 K, and 900 K. It can be seen that, for both cases, the power factor depends on the temperature. For ZnO, the highest peaks are located very near to the Fermi level and the corresponding maximum PF values decrease from 8×10^{11} W/K²ms at 300 K to 2×10^{11} W/K²ms at 900 K. For 2 at. %AZO, the peak

positions shifted towards lower chemical potential (−1.75 eV) with the maximum S values decreasing from 2.9×10^{11} W/K²ms at 300 K to 1.4×10^{11} W/K²ms at 900 K.

Figure 11c, d illustrates the figure of merit as a function of chemical potential for (c) pure ZnO and (d) AZO at different temperatures. Both structures show two high peaks whose maximum values approach unity at room temperature. Thus, these materials can be considered as good thermoelectric devices for which ZT should be as close to unity as possible [53, 93, 94]. As the temperature increases up to 900 K, the peaks slightly decrease down to ~0.8.

Fig. 11 Power factor (a and b) and figure of merit (c and d) as a function of chemical potential of pure ZnO and 2 at. % AZO



Conclusions

Structural, electronic, optical, and thermoelectric properties of pure and Al-doped zinc oxide were numerically deduced, analyzed and compared, using Wien2k package. We considered the most stable wurtzite ZnO structure and adopted a hexagonal $2 \times 2 \times 6$ supercell that includes 48 oxygen atoms and 48 zinc atom into which one Zn atom is substituted by an Al atom; thus corresponding to $\sim 2\%$ at. Al concentration. It was first shown that the combination of GGA and mBJ gives more accurate results than other tested approximations and consequently is adopted for this investigation. Several interesting results were deduced. The AZO cell parameters decreased leading to a decrease in the supercell volume as a result of the large difference in electronegativity and atomic radii of Zn and Al atoms. The deduced direct band gap of ZnO, 2.81 eV, increased up to 3.3 eV for 2 at. % AZO.

The dielectric function of pure ZnO showed a fluctuation whose threshold occurs at 2.81 eV representing the direct optical transitions between the valence band maximum and the first minimum conduction band. Whereas, for 2 at. % AZO, two main differences with pure ZnO were noticed (i) at lower energies the appearance of an extra strong fluctuation in $\epsilon_1(\omega)$ and a high peak for $\epsilon_2(\omega)$ curves and (ii) a wider optical band gap of 3.3 eV.

The reflectivity for both materials showed an overall tendency consisting of a very slow intensification of up to 11 eV followed by a very sharp increase beyond this value. However, for the 2 at. % AZO, a new high peak with $R(\omega)_{zz}$ curve appeared at 0.96 eV, which could be due to the new impurity band introduced by Al doping. Moreover, the doping effect seems to slightly lower the reflectivity values by ~ 1.17 for xx-polarization and ~ 1.45 for zz-polarization; a similar decreasing tendency for 6 at. % AZO was found to be about twice less than that of pure ZnO [85]. For the optical absorption, besides the overall curve similarities for pure and doped ZnO, it is observed for the latter that (i) the absorption coefficient is higher in the range [3.1–6.2eV], (ii) an important absorption (strong peak) along the zz direction occurs in the IR, and (iii) a small blue shift phenomenon is obtained in the 2 at. % AZO.

For thermoelectric properties, we investigated the effects of chemical potential on Seebeck coefficient, electrical and thermal conductivities, power factor, and figure of merit at temperatures varying from 300 K to 900 K, for ZnO and 2 at. % AZO. The deduced high Seebeck coefficient values, $|S_{ZnO}| = 1.16$ mV/K and $|S_{AZO}| = 0.746$ mV/K, indicate that pure and doped ZnO represent good thermoelectric materials. The trends of variations of electrical and thermal conductivities with chemical potential are quite similar in the range 300 to 900 K for both structures: an initial decrease followed by a low saturation region and then a final increase.

However, while the temperature has very negligible effect on the electrical conductivity, it strongly affects the thermal conductivity. In fact as T increases from 300 to 900 K, κ/τ decreases from 2×10^{16} W/mKs to 4.5×10^{15} W/mKs for ZnO and from $\sim 3 \times 10^{15}$ W/mKs at $T = 300$ K to 0.5×10^{15} W/mKs at 2 at. % AZO. Finally, the value of the figure of merit approaches, at room temperature, unity which is the highest possible value indicating that both ZnO and AZO material can be considered as good thermoelectric device.

Author contributions NEAD, MD, and DB were involved in investigations and TT and SC in supervising. All authors have contributed and agreed to the published version of the manuscript.

Declarations

Competing interests The authors declare no competing interests.

References

- Galazka Z (2020) Transparent semiconducting oxides: bulk crystal growth and fundamental properties. Jenny Stanford Publishing CRC Press
- Xu R, Min L, Qi Z, Zhang X, Jian J, Ji Y, Qian F, Fan J, Kan C, Wang H, Tian W, Li L, Li W, Yang H (2020) Perovskite transparent conducting oxide for the design of a transparent, flexible, and self-powered perovskite photodetector. *ACS Appl Mater Interfaces* 12(14):16462–16468. <https://doi.org/10.1021/acsami.0c01298>
- Chavan GT, Kim Y, Khokhar MQ, Hussain SQ, Cho EC, Yi J, Ahmad Z, Rosaiah P, Jeon CW (2023) A brief review of transparent conducting oxides (TCO): the influence of different deposition techniques on the efficiency of solar cells. *Nanomaterials* 13(7):1226. <https://doi.org/10.3390/nano13071226>
- Ginley DS, Perkins JD, Ginley DS (2011) Handbook of transparent conductors. Springer, US, p 2011
- Minami T (2005) Transparent conducting oxide semiconductors for transparent electrodes. *Semicond Sci Technol* 20(4):S35–S44. <https://doi.org/10.1088/0268-1242/20/4/004>
- Kathwate LH, Umadevi G, Kulal PM, Nagaraju P, Dubal DP, Nanjundan AK, Mote VD (2020) Ammonia gas sensing properties of Al doped ZnO thin films. *Sens Actuators A Phys* 313:112193. <https://doi.org/10.1016/j.sna.2020.112193>
- Vidor FF, Wirth GI, Hilleringmann U (2018) ZnO thin-film transistors for cost-efficient flexible electronics. Springer Inter Pub, Germany
- Özgür Ü, Alivov YI, Liu C, Teke A, Reshchikov M, Doğan S, Morkoç AH (2005) A comprehensive review of ZnO materials and devices. *J Appl Phys* 98(4):041301. <https://doi.org/10.1063/1.1992666>
- Nagar S, Chakrabarti S (2017) Optimisation of ZnO thin films: implants, properties, and device fabrication. Springer, Singapore
- Meena J, Pavithra G, Anusha D, Kumar AS, Santhakumar K (2023) The green approach of ZnO NPs and its antioxidant, hemolytic, and photocatalytic activity and functionalized r-GO-ZnO for energy storage application. *J Mater Sci Mater Electron* 34(14):1131. <https://doi.org/10.1007/s10854-023-10373-2>
- Liu Y, Wan H, Islam M, Hasan KF, Cao S, Wang Z, Xiong Y, Lü S, Lü H, Mahmud S (2022) Liquid exfoliated Bi₂S₃ nanosheets

- as photocatalysts for degradation of azo dyes and detoxification of hexavalent chromium. *Mater Sci Engin B* 285:115898. <https://doi.org/10.1016/j.mseb.2022.115898>
12. Arumugasamy SK, Ramakrishnan S, Yoo DJ, Govindaraju S, Yun K (2022) Tuning the interfacial electronic transitions of bi-dimensional nanocomposites (pGO/ZnO) towards photocatalytic degradation and energy application. *Enviro Res* 204:112050. <https://doi.org/10.1016/j.envres.2021.112050>
 13. Vidor FF, Wirth GI, Hilleringmann U (2018) ZnO thin-film transistors for cost-efficient flexible electronics. Springer International Publishing. <https://doi.org/10.1007/978-3-319-72556-7>
 14. Feng ZC (2012) Handbook of Zinc Oxide and Related Materials: two volume, devices and nano-engineering. CRC Press
 15. Gopalakrishnan S, Shankar R, Pazhanivel T, Priyadharshini M, Maiyalagan T (2003) Optoelectronic properties of hollow spheroid (ZnO)_m quantum dots with nanotube (carbon and ZnO) nanocomposites in the solvent phase – A DFT/TD-DFT study. *Mater Sci Engin B* 287:116129. <https://doi.org/10.1016/j.mseb.2022.116129>
 16. Shanmugam NR, Muthukumar S, Prasad S (2017) A review on ZnO-based electrical biosensors for cardiac biomarker detection. *Future Sci OA* 3(4):FSO196. <https://doi.org/10.4155/foa-2017-0006>
 17. Luu SDN, Duong TA, Phan TB (2019) Effect of dopants and nanostructuring on the thermoelectric properties of ZnO materials. *Adv Nat Sci: Nanosci Nanotechnol* 10(2):023001. <https://doi.org/10.1088/2043-6254/ab22ad>
 18. Hashir P, Pradyumnal PP, Wani AF, Kaur K (2022) Experimental and first-principles thermoelectric studies of bulk ZnO. *Conf Ser: Mater Sci Eng* 1263(1):12025. <https://doi.org/10.1088/1757-899X/1263/1/012025>
 19. Ashrafi A, Jagadish C (2007) Review of zincblende ZnO: stability of metastable ZnO phases. *J Appl Phys* 102(7):0711014. <https://doi.org/10.1063/1.2787957>
 20. Khuili M, Fazouan N, Abou El Makarim H (2015) DFT study of physical properties of wurtzite, zinc blende, and rocksalt phases of zinc oxide using GGA and TB-mBJ potential. 3rd International Renewable and Sustainable Energy Conference (IRSEC) 1–4, Marrakech. <https://doi.org/10.1109/IRSEC.2015.7454962>
 21. Shabbir S, Shaari A, Haq BU, Ahmed R, Ahmed M (2020) Investigations of novel polymorphs of ZnO for optoelectronic applications. *Optik* 206:164285. <https://doi.org/10.1016/j.ijleo.2020.164285>
 22. Feng C, Chen Z, Li W, Zhang F, Li X, Xu L, Sun M (2019) First-principle calculation of the electronic structures and optical properties of the metallic and nonmetallic elements-doped ZnO on the basis of photocatalysis. *Physica B: Condens Matter* 555:53–60. <https://doi.org/10.1016/j.physb.2018.11.043>
 23. Qi K, Xing X, Zada A, Li M, Wang Q, Liu SY, Wang G (2020) Transition metal doped ZnO nanoparticles with enhanced photocatalytic and antibacterial performances: Experimental and DFT studies. *Ceram Int* 46(2):1494–1502. <https://doi.org/10.1016/j.ceramint.2019.09.116>
 24. Hou Q, Jia XF, Xu ZC, Zhao CW, Qu LF (2018) Effects of Li doping and point defect on the magnetism of ZnO. *Ceram Int* 44(2):1376–1383. <https://doi.org/10.1016/j.ceramint.2017.09.002>
 25. Daksh D, Agrawal YK (2016) Rare earth-doped zinc oxide nanostructures: a review. *Rev Nanosci Nanotechnol* 5(1):1–27. <https://doi.org/10.1166/rnn.2016.1071>
 26. Ren J, Wu JX, Liu PP (2023) Controlling the electronic and magnetic properties of ZnO monolayer by rare-earth atoms substitutional doping. *Physica B: Condens Matter* 414661. <https://doi.org/10.1016/j.physb.2023.414661>
 27. Pathak TK, Swart HC, Kroon RE (2018) Structural and plasmonic properties of noble metal doped ZnO nanomaterials. *Physica B: Condens Matter* 535:114–118. <https://doi.org/10.1016/j.physb.2017.06.074>
 28. Hou Q, Xi DM, Li WL, Jia XF, Xu ZC (2018) First-principles research on the optical and electrical properties and mechanisms of In-doped ZnO. *Physica B: Condens Matter* 537:258–266. <https://doi.org/10.1016/j.physb.2018.02.026>
 29. Wu M, Yu S, Chen G, He L, Yang L, Zhang W (2015) Structural, optical, and electrical properties of Mo-doped ZnO thin films prepared by magnetron sputtering. *Appl Surf Sci* 324:791–796. <https://doi.org/10.1016/j.apsusc.2014.11.039>
 30. Tsay CY, Cheng HC, Tung YT, Tuan WH, Lin CK (2008) Effect of Sn-doped on microstructural and optical properties of ZnO thin films deposited by sol–gel method. *Thin Solid Films* 517(3):1032–1036. <https://doi.org/10.1016/j.tsf.2008.06.030>
 31. Yang J, Jiang Y, Li L, Gao M (2017) Structural, morphological, optical and electrical properties of Ga-doped ZnO transparent conducting thin films. *Appl Surf Sci* 421:446–452. <https://doi.org/10.1016/j.apsusc.2016.10.079>
 32. Li C, Hou Q (2018) Effects of Y doping with point defects on the ferromagnetic properties of ZnO (0001)-Zn polar surface. *Appl Surf Sci* 459:393–396. <https://doi.org/10.1016/j.apsusc.2018.08.012>
 33. Jia XF, Hou QY, Xu ZC, Qu LF (2018) Effect of Ce doping on the magnetic and optical properties of ZnO by the first principle. *J Magn Magn Mater* 465:128–135. <https://doi.org/10.1016/j.jmmm.2018.05.037>
 34. Khuili M, Fazouan N, Abou El Makarim H, Atmani EH, Abbassi A, Rai DP (2020) (Li,F) co-doped ZnO: optoelectronic devices applications. *Superlattices Microstruct* 145:106645. <https://doi.org/10.1016/j.spmi.2020.106645>
 35. El Hallani G, Fazouan N, Liba A, Khuili M (2016) The effect of sol aging time on Structural and Optical properties of sol gel ZnO doped Al. *J Phys: Conf Ser* 758(1):2021. <https://doi.org/10.1088/1742-6596/758/1/012021>
 36. Khuili M, Fazouan N, Abou El Makarim H, Atmani EH, Houmad M (2020) Improvement of optical properties of Mg doped ZnO by nanostructuring for applications in optoelectronics. *Mater Res Express* 7(2):025043. <https://doi.org/10.1088/2053-1591/ab748b>
 37. Li D, Huang JF, Cao LY, Jia-Yin LI, OuYang HB, Yao CY (2014) Microwave hydrothermal synthesis of Sr²⁺ doped ZnO crystal-lites with enhanced photocatalytic properties. *Ceram Int* 40:2647–2653. <https://doi.org/10.1016/j.ceramint.2013.10.061>
 38. Anandh BA, Shankar Ganesh A, Sakthivel R, Tamilselvan K, Kanusamy R (2018) Structural, morphological and optical properties of aluminium doped ZnO thin film by dip-coating method. *Orient J Chem* 34(3):1619–1624. <http://ir.psgcas.ac.in/id/eprint/254>
 39. El hamali SO, Cranton WM, Kalfagiannis N, Hou X, Ranson R, Koutsogeorgis DC (2016) Enhanced electrical and optical properties of room temperature deposited Aluminium doped Zinc Oxide (AZO) thin films by excimer laser annealing. *Opt Lasers Eng* 80:45–51. <https://doi.org/10.1016/j.optlaseng.2015.12.010>
 40. Karim MR, Sheikh MRK, Yahya R, Salleh NM, Azzahari AD (2015) Synthesis of polymerizable liquid crystalline monomers and their side chain liquid crystalline polymers bearing azo-ester linked benzothiazole mesogen. *Colloid Polym Sci* 293:1923–1935. <https://doi.org/10.1007/s00396-015-3578-8>
 41. Yan X, Ma J, Xu H, Wang C, Liu Y (2016) Fabrication of silver nanowires and metal oxide composite transparent electrodes and their application in UV light-emitting diodes. *J Physics D: Appl Phys* 49(32):325103. <https://doi.org/10.1088/0022-3727/49/32/325103>
 42. Porrawatkul P, Nuengmatcha P, Kuyyogsuy A, Pimsen R, Rattanaburi P (2023) Effect of Na and Al doping on ZnO nanoparticles for potential application in sunscreens. *J Photochem Photobiol B: Biol* 240:112668. <https://doi.org/10.1016/j.jphotobiol.2023.112668>

43. Zarhri Z, Dzul MBC, Ziat Y, Torrez LFI, Oubram O, Ifguis O (2022) Comparative study of optical properties of ZnO Zinc blend and rock salt structures, TB- mBJ and GGA approximations. *Physica B: Condens Matter* 634:413798. <https://doi.org/10.1016/j.physb.2022.413798>
44. Achehboune M, Khenfouch M, Boukhoubza I, Leontie L, Doroftei C, Carlescu A, Bulai G, Mothudi B, Zorkani I, Jorio A (2022) Microstructural, FTIR and Raman spectroscopic study of rare earth doped ZnO nanostructures. *Mater Today: Proc* 53:319–323. <https://doi.org/10.1016/j.matpr.2021.04.144>
45. Singh R, Mukherjee SK (2022) Correlation of structural, electrical and optical properties of Al-doped ZnO TCOs. *J Mater Sci: Mater Electron* 33(9):6969–6980. <https://doi.org/10.1007/s10854-022-07876-9>
46. Abd Hamid NE, Abdullah MH, Yusoff MZM, Azurahaman C, Abdullah C (2022) Simulation of metal contacts on the Al doped ZnO photoconductive sensor. *Int J Electroactive Mater* 10:12–17 <https://www.electroactmater.com/index.php/volume-10-2022?id=60&subid=426>
47. Doghmane NEA, Chettibi S, Challali F, Chelouche A, Touam T (2022) Confocal magnetron sputtering deposition of Cu/AZO bilayer structures: effect of Cu thickness on microstructural and optoelectronic properties. *J Mater Sci: Mater Electron* 33(36):26717–26727. <https://doi.org/10.1007/s10854-022-09338-8>
48. Blaha P, Schwarz K, Madsen GH, Kvasnicka D, Luitz J (2001) wien2k. An augmented plane wave+ local orbitals program for calculating crystal properties, *Techn WIEN2K*. Austria 60:1
49. Perdew JP, Burke K, Ernzerhof M (1996) Quantum theory group tulane university. *Phys Rev Lett* 77(18):3865–3868. <https://doi.org/10.1103/PhysRevLett.77.3865>
50. Jellal I, Ahmoum H, Khaissa Y, Nouneh K, Boughrara M, Fahoume M, Chopra S, Naja J (2019) Experimental and ab-initio investigation of the microstructure and optoelectronic properties of FCM-CVD-prepared Al-doped ZnO thin films. *Appl Phys A* 125:1–7. <https://doi.org/10.1007/s00339-019-2947-4>
51. Tran F, Blaha P (2009) Accurate band gaps of semiconductors and insulators with a semilocal exchange-correlation potential. *Phys Rev Lett* 102(22):226401–226404. <https://doi.org/10.1103/PhysRevLett.102.226401>
52. Momma K, Izumi F (2011) VESTA 3 for three-dimensional visualization of crystal, volumetric and morphology data. *J Appl Crystallogr* 44(6):1272–1276. <https://doi.org/10.1107/S0021889811038970>
53. Khuili M, Bounbaa M, Fazouan N, Elmakarim HA, Sadiki Y, Al-Qaisi S, Allaoui I, Maskar E, Chahid EH, Maher K, Abba EH (2023) First-principles study of structural, elastic, optoelectronic and thermoelectric properties of B-site-ordered quadruple perovskite Ba₄Bi₃NaO₁₂. *J Solid State Chem* 322:123955. <https://doi.org/10.1016/j.jssc.2023.123955>
54. Achehboune M, Khenfouch M, Boukhoubza I, Derkaoui I, Mothudi BM, Zorkani I, Jorio A (2021) Effect of Yb concentration on the structural, magnetic and optoelectronic properties of Yb doped ZnO: first principles calculation. *Opt Quantum Electron* 53:1–14. <https://doi.org/10.21203/rs.3.rs-877060/v1>
55. Valdez LA, Caravaca MA, Casali RA (2019) Ab-initio study of elastic anisotropy, hardness and volumetric thermal expansion coefficient of ZnO, ZnS, ZnSe in wurtzite and zinc blende phases. *J Phys Chem Solids* 134:245–254. <https://doi.org/10.1016/j.jpcs.2019.05.019>
56. Kisi EH, Elcombe MM (1989) u parameters for the wurtzite structure of ZnS and ZnO using powder neutron diffraction. *Acta Crystallograph C: Cryst Struct Commun* 45(12):1867–1870. <https://doi.org/10.1107/S0108270189004269>
57. Farhat S, Rekaby M, Awad R (2018) Synthesis and characterization of Er-doped nano ZnO samples. *J Supercond Nov Magn* 31:3051–3061. <https://doi.org/10.1007/s10948-017-4548-9>
58. Bouhouche S, Bensouici F, Toubane M, Azizi A, Otmani A, Chebout K, Kezzoula F, Tala-Ighil R, Bououdina M (2018) Effect of Er³⁺ doping on structural, morphological and photocatalytic properties of ZnO thin films. *Mater Res Express* 5(5):056407. <https://doi.org/10.1088/2053-1591/aac4e8>
59. Naik EI, Naik HSB, Viswanath R, Kirthan BR, Prabhakara MC (2020) Effect of zirconium doping on the structural, optical, electrochemical and antibacterial properties of ZnO nanoparticles prepared by sol-gel method. *Chem Data Collect* 29:100505. <https://doi.org/10.1016/j.cdc.2020.100505>
60. Meng Z, Mo X, Cheng X, Zhou Y, Tao X, Ouyang Y (2017) Interactions between Er dopant and intrinsic point defects of ZnO: a first-principles study. *Mater Res Express* 4:035903. <https://doi.org/10.1088/2053-1591/aa6292>
61. Khuili M, Fazouan N, Abou El Makarim H, Atmani EH, Rai DP, Houmad M (2020) First-principles calculations of rare earth (RE=Tm, Yb, Ce) doped ZnO: Structural, optoelectronic, magnetic, and electrical properties. *Vacuum* 181:109603. <https://doi.org/10.1016/j.vacuum.2020.109603>
62. John R, Padmavathi S (2016) Ab initio calculations on structural, electronic and optical properties of ZnO in wurtzite phase. *Cryst Str Theory Appl* 5(2):24–41. <https://doi.org/10.4236/csta.2016.52003>
63. Desgreniers S (1998) High-density phases of ZnO: Structural and compressive parameters. *Phys Rev B* 58(21):14102. <https://doi.org/10.1103/PhysRevB.58.14102>
64. Decremps F, Datchi F, Saitta AM, Polian A, Pascarelli S, Di Cicco A, Baudelet F (2003) Local structure of condensed zinc oxide. *Phys Rev B* 68(10):104101. <https://doi.org/10.1103/PhysRevB.68.104101>
65. Charifi Z, Baaziz H, Hussain Reshak A (2007) Ab-initio investigation of structural, electronic and optical properties for three phases of ZnO compound. *Phys Status Solidi (b)* 244(9):3154–3167. <https://doi.org/10.1002/pssb.200642471>
66. Karzel H, Potzel W, Köfferlein M, Schiessl W, Steiner M, Hiller U, Kalvius GM, Blaha P, Schwarz K, Pasternak MP (1996) Lattice dynamics and hyperfine interactions in ZnO and ZnSe at high external pressures. *Phys Rev B* 53(17):11425–11438. <https://doi.org/10.1103/PhysRevB.53.11425>
67. Sivaganesh D, Saravanakumar S, Sivakumar V, Syed Ali KS, Akapo E, Alemayehu E, Rajajeyaganthan R, Saravanan R (2019) Structural, optical and charge density analysis of Al doped ZnO Materials. *J Mater Sci: Mater Electron* 30(3):2966–2974. <https://doi.org/10.1007/s10854-018-00574-5>
68. Pham ATT, Vo PTN, Ta HKT, Pham NK, Lai HT, Tran HNT, Tran VC, Doan TLH, Park S, Phan TB (2020) Dopants and induced residual stress-controlled thermoelectric properties of ZnO thin films. *Mater Sci Eng: B* 261:114712. <https://doi.org/10.1016/j.mseb.2020.114712>
69. Xiao H, Tahir-Kheli J, Goddard III WA (2011) Accurate band gaps for semiconductors from density functional theory. *J Phys Chem Lett* 2(3):212–217. <https://doi.org/10.1021/jz101565j>
70. López-Mena ER, Ceballos-Sanchez O, Hooper TJN, Sanchez-Ante G, Rodríguez-Muñoz M, Renteria-Salcedo JA, Sanchez-Martinez A (2021) The effect of Yb doping on ZnO thin films obtained via a low-temperature spin coating method. *J Mater Sci: Mater Electron* 32:347–359. <https://doi.org/10.1007/s10854-020-04785-7>
71. Alkahtani EA, Merad AE, Boufatah MR, Benosman A (2017) DFT investigation of structural, electronic and optical properties of pure and Er-doped ZnO: Modified Becke-Johnson exchange potential. *Optik* 128:274–280. <https://doi.org/10.1016/j.ijleo.2016.10.032>
72. Dixit H, Saniz R, Lamoen D, Partoens B (2010) The quasiparticle band structure of zincblende and rocksalt ZnO. *J Physics: Condens Matter* 22:125505. <https://doi.org/10.1088/0953-8984/22/12/125505>
73. Oba F, Togo A, Tanaka I, Paier J, Kress G (2008) Defect energetics in ZnO: a hybrid Hartree-Fock density functional study. *Phys Rev B* 77(2008):245202–245206 <http://hdl.handle.net/2433/84635>

74. Boufatah MR, Merad AE (2014) Structural stability, elastic and electronic properties of zincblende $(\text{GaN})_1/(\text{ZnO})_1$ superlattice: Modified Becke–Johnson exchange potential. *Mater Sci Semicond Process* 19:179–185. <https://doi.org/10.1016/j.mssp.2013.12.022>
75. Wang M, Lee KE, Hahn SH, Kim EJ, Kim S, Chung JS, Park C (2016) Optical and photoluminescent properties of sol-gel Al-doped ZnO thin films. *Mater Lett* 61(4–5):1118–1121. <https://doi.org/10.1016/j.matlet.2006.06.065>
76. Burstein E (1954) Anomalous optical absorption limit in InSb. *Phys Rev* 93:632–633. <https://doi.org/10.1103/PhysRev.93.632>
77. Moss T (1954) The interpretation of the properties of indium antimonide. *Proc Phys Soc B* 67:775–782. <https://doi.org/10.1088/0370-1301/67/10/306>
78. Dixon SC, Scanlon DO, Carmalt CJ, Parkin IP (2016) n-Type doped transparent conducting binary oxides: an overview. *J Mater Chem C* 4(29):6946–6961. <https://doi.org/10.1039/C6TC01881E>
79. Sernelius BE, Berggren KF, Jim ZC, Hamberg I, Granqvist CG (1988) Band-gap tailoring of ZnO by means of heavy Al doping. *Phys Rev B* 37:10244–10248. <https://doi.org/10.1103/PhysRevB.37.10244>
80. Darma Y, Setiawan FG, Majidi MA, Rusydi A (2015) Theoretical investigation on electronic properties of ZnO crystals using DFT-based calculation method. *Adv Mater Res* 1112:41–44. <https://doi.org/10.4028/www.scientific.net/AMR.1112.41>
81. Pachau Z (2023) First principle study of electronic, optical and thermoelectric properties of CuInS_2 and CuInSe_2 . *Indian J Pure Appl Phys* 61(2):108–114. <https://doi.org/10.56042/ijpap.v61i2.67985>
82. Li L, Wang W, Liu H, Liu X, Song Q, Ren S (2009) First principles calculations of electronic band structure and optical properties of Cr-doped ZnO. *J Phys Chem C* 113(19):8460–8464. <https://doi.org/10.1021/jp811507r>
83. Saha S, Sinha TP, Mookerjee A (2000) Electronic structure, chemical bonding, and optical properties of paraelectric BaTiO_3 . *Phys Rev B* 62(13):8828. <https://doi.org/10.1103/PhysRevB.62.8828>
84. Reshak AH, Kityk IV, Ebothe J, Fedorchuk AO, Fedyna MF, Kamarudin H, Auluck S (2013) Crystallochemical affinity and optical functions of ZrGa_2 and ZrGa_3 compounds. *J Alloys Compd* 546:14–19. <https://doi.org/10.1016/j.jallcom.2012.08.073>
85. Jin Z, Qiao L, Guo C, He Z, Liu L, Rong M (2016) First-principles study of electrical and optical properties of (Al,Sn) co-doped ZnO. *Optik* 127(4):1988–1992. <https://doi.org/10.1016/j.ijleo.2015.10.224>
86. Li Y, Hou QY, Wang XH, Kang HJ, Yaer X, Li JB, Wang TM, Miao L, Wang J (2019) First-principles calculations and high thermoelectric performance of La–Nb doped SrTiO_3 ceramics. *J Mater Chem A* 7(1):236–247. <https://doi.org/10.1039/C8TA10079A>
87. Al-Qaisi S, Rached H, Alrebdi TA, Bouzgarrou S, Behera D, Mukherjee SK, Khuili M, Adam M, Verma AS, Ezzeldien M (2023) Study of mechanical, optical, and thermoelectric characteristics of Ba_2XMoO_6 ($\text{X}=\text{Zn}, \text{Cd}$) double perovskite for energy harvesting. *J Comput Chem*. <https://doi.org/10.1002/jcc.27209>
88. Goldsmid HJ (2016) *Introduction to Thermoelectricity*. Springer-Verlag, Berlin
89. Maskar E, Fakhim Lamrani A, Belaiche M, Es-Smairi A, Khuili M, Al-Qaisi S, Vu TV, Rai DP (2021) Electronic, magnetic, optical and transport properties of wurtzite-GaN doped with rare earth (RE= Pm, Sm, and Eu): First principles approach. *Surf Interfaces* 24:101051. <https://doi.org/10.1016/j.surfin.2021.101051>
90. Ohtaki M (2010) Oxide thermoelectric materials for heat-to-electricity direct energy conversion. *Kyushu University Global COE Program Novel Carbon Resources Sciences Newsletter*, pp 3–8
91. Yang J, Xi L, Qiu W, Wu L, Shi X, Chen L, Singh DJ (2016) On the tuning of electrical and thermal transport in thermoelectrics: an integrated theory–experiment perspective. *NPJ Comput Mater* 2(1):1–17. <https://doi.org/10.1038/npjcompumats.2015.15>
92. Siddique M, Rahman AU, Iqbal A, Haq BU, Azam S, Nadeem A, Qayyum A (2019) A systematic first-principles investigation of structural, electronic, magnetic, and thermoelectric properties of thorium monopnictides Th Pn (Pn= N, P, As): a comparative analysis of theoretical predictions of LDA, PBEsol, PBE-GGA, WC-GGA, and LDA+ U Methods. *Int J Thermophys* 40(104):1–21. <https://doi.org/10.1007/s10765-019-2572-7>
93. Sun J, Wang HT, He J, Tian Y (2005) Ab initio investigations of optical properties of the high-pressure phases of ZnO. *Phys Rev B* 71(12):125132–125136. <https://doi.org/10.1103/PhysRevB.71.125132>
94. Takeuchi T (2009) Conditions of electronic structure to obtain large dimensionless figure of merit for developing practical thermoelectric materials. *Mater Trans* 50(10):2359–2365. <https://doi.org/10.2320/matertrans.M2009143>

Publisher's Note Springer Nature remains neutral with regard to jurisdictional claims in published maps and institutional affiliations.

Springer Nature or its licensor (e.g. a society or other partner) holds exclusive rights to this article under a publishing agreement with the author(s) or other rightsholder(s); author self-archiving of the accepted manuscript version of this article is solely governed by the terms of such publishing agreement and applicable law.